

# Star Formation News Letter

No. 299 #36–40, 46–50

楠根貴成 (国立天文台)

#36 ALMA Reveals Sequential High-mass Star Formation in the G9.62+0.19 Complex

#38 A turbulent origin for the complex envelope kinematics in the young low-mass core Per-Bolo 58

#40 The Seahorse Nebula: New views of the filamentary infrared dark cloud G304.74+01.32 from SABOCA, Herschel, and WISE

# #36 ALMA Reveals Sequential High-mass Star Formation in the G9.62+0.19 Complex

Tie Liu<sup>1,2,3,4</sup> , John Lacy<sup>5</sup> , Pak Shing Li<sup>6</sup>, Ke Wang<sup>7</sup> , Sheng-Li Qin<sup>8</sup> , Qizhou Zhang<sup>9</sup> , Kee-Tae Kim<sup>1</sup> , Guido Garay<sup>10</sup>, Yuefang Wu<sup>11</sup>, Diego Mardones<sup>10</sup> , Qingfeng Zhu<sup>12</sup> , Ken'ichi Tatematsu<sup>13</sup> , Tomoya Hirota<sup>13</sup> , Zhiyuan Ren<sup>14</sup>, Sheng-Yuan Liu<sup>15</sup> , Hwei-Ru Chen<sup>15</sup> , Yu-Nung Su<sup>15</sup>, and Di Li<sup>14,16</sup>

1. G9.62クランプ： HII領域(B・C)のPDRに囲まれている

2. ALMA 1.3mm： 高密度コア12個同定

- 4 - 87 Msun
- 星なしコア - UCHII領域

連続的な星形成を示唆

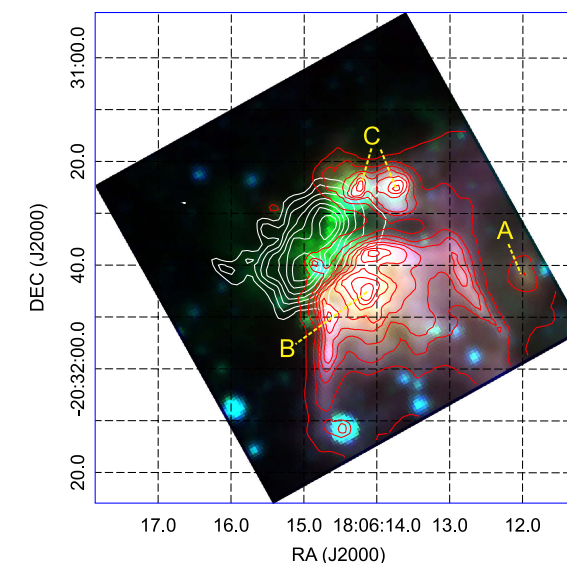


**Figure 1.** *Spitzer*/IRAC three-color composite image ( $8\ \mu\text{m}$  in red,  $4.5\ \mu\text{m}$  in green, and  $3.6\ \mu\text{m}$  in blue) of the G9.62+0.19 complex. The *Spitzer*/IRAC  $8\ \mu\text{m}$  emission is also shown by the red contours. The contour levels are  $(0.1, 0.2, 0.3, 0.4, 0.5, 0.6, 0.7, 0.8, 0.9) \times 2550\ \text{MJy/sr}$ . The JCMT/SCUBA  $450\ \mu\text{m}$  emission from the G9.62 clump is shown by the white contours. The contour levels are  $(0.3, 0.4, 0.5, 0.6, 0.7, 0.8, 0.9) \times 96\ \text{Jy/beam}$ . A, B, and C are the three evolved H II regions.

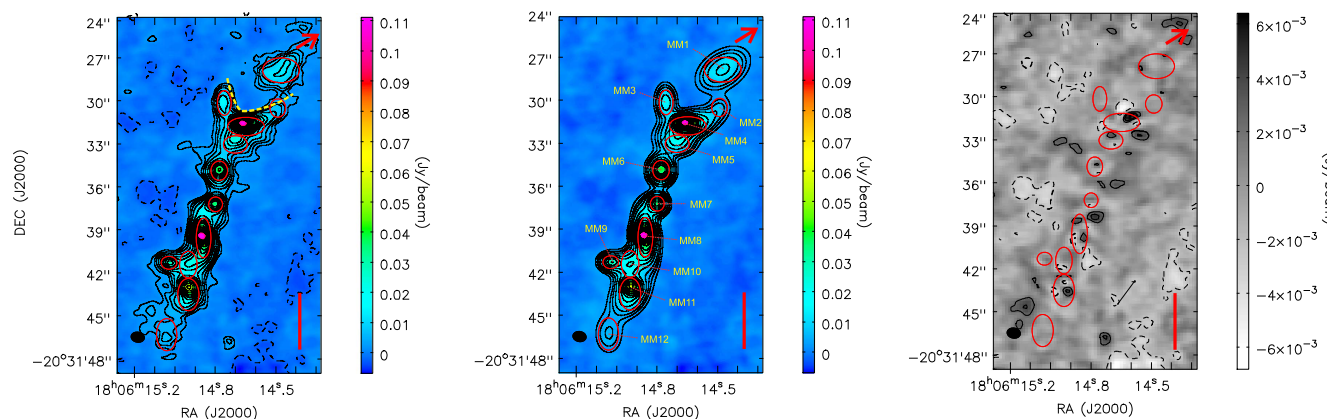


**Figure 2.** 1.3 mm continuum from ALMA observations. The red ellipses represent the dense cores identified from the 2D Gaussian fit. The black filled ellipse represents the beam. The vertical red line represents a spatial scale of 0.1 pc. The position of radio source “C” is marked by an arrow. Left panel: observed image; the contours are  $(-3, 3, 5, 7, 10, 15, 20, 25, 30, 35, 40, 50, 60, 70, 80, 90, 100, 110) \times 0.8\ \text{mJy/beam}$ . As depicted by the yellow dashed curve, the northern part of the G9.62 clump is very likely bent by the compression of the H II region “C.” Middle panel: fitted image; the contours are  $(3, 5, 7, 10, 15, 20, 25, 30, 35, 40, 50, 60, 70, 80, 90, 100, 110) \times 0.8\ \text{mJy/beam}$ . Right: residual image; the contours are  $(-3, 3, 5) \times 0.8\ \text{mJy/beam}$ .

3. うち3つでOutflowを検出 in SiO (5-4) or CO (2-1)： MM6, MM7/G, MM8/F

# Accretion rate

MM6 : 若く (~8.5 x 10<sup>3</sup> yr)、collimateしたoutflow

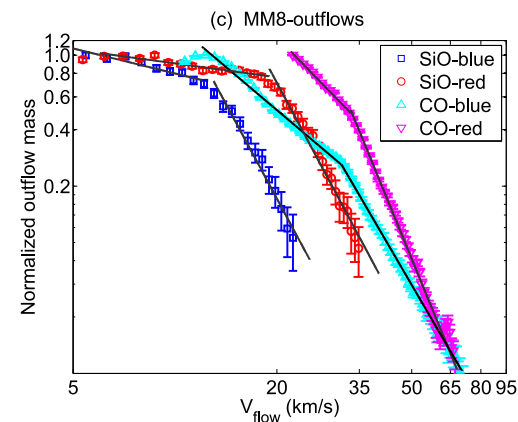
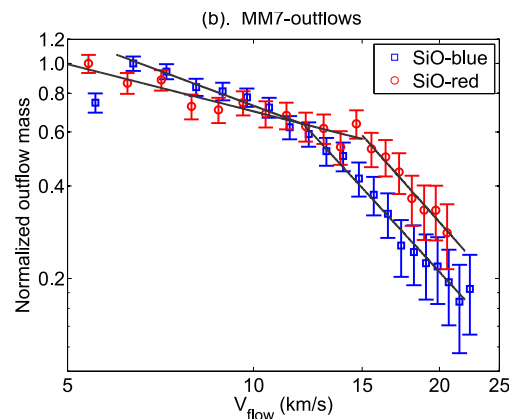
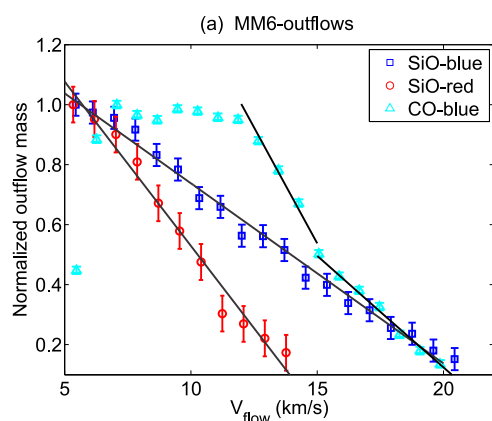
3.9 x 10<sup>-4</sup>

MM7/G : inclinationが非常に小さい

5.7 x 10<sup>-5</sup>

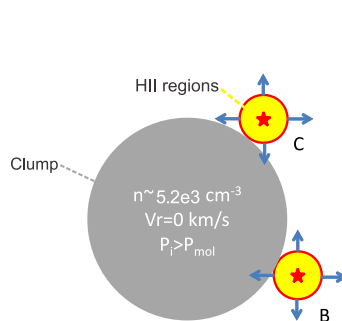
MM8/F : 100km s<sup>-1</sup>と非常に活発

2.2 x 10<sup>-3</sup> Msun yr<sup>-1</sup>

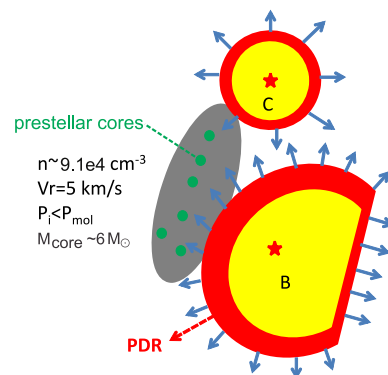


7. 他のMassiveクランプよりも、高い星形成効率・ガスの枯渇時間が短い  
G6.92には低質量星がほとんどない

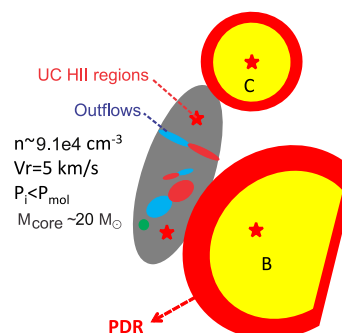
=> HII領域からのfeedbackが星形成効率を上昇・低質量星形成を抑制



(a). Compression phase



(b). Fragmentation phase



(c). Accretion phase

# #38 A Turbulent Origin for the Complex Envelope Kinematics in the Young Low-mass Core Per-bolo 58

María José Maureira<sup>1</sup>, Héctor G. Arce<sup>1</sup> , Stella S. R. Offner<sup>2</sup> , Michael M. Dunham<sup>3</sup> , Jaime E. Pineda<sup>4</sup> ,  
Manuel Fernández-López<sup>5</sup>, Xuepeng Chen<sup>6</sup>, and Diego Mardones<sup>7</sup> 

目的： 深く埋もれたfirst core候補Per-bolo 58周辺の envelopeの構造や力学を調べる

観測： CARMAを使用。3 mm 連続光、NH<sub>2</sub>D(1<sub>1,1</sub>-1<sub>0,1</sub>)、N<sub>2</sub>H<sup>+</sup>(1-0)、HCN(1-0)、HCO<sup>+</sup>(1-0) の分子輝線マップ@ 分解能 ~1000 au

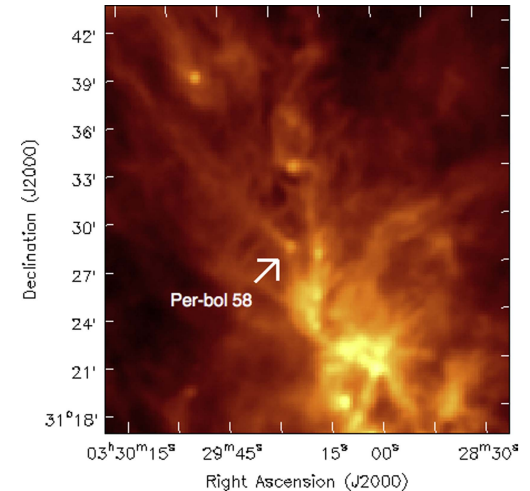


Figure 1. *Herschel* 250  $\mu\text{m}$  map of the NGC 1333 region in Perseus. The white arrow indicates the position of the dense core Per-bolo 58.

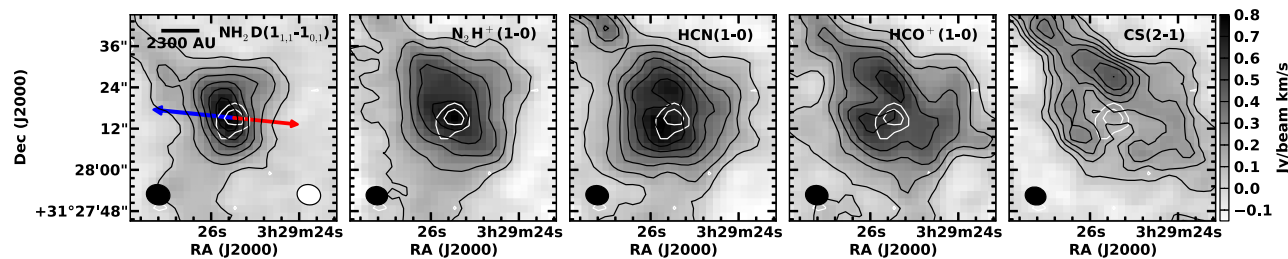
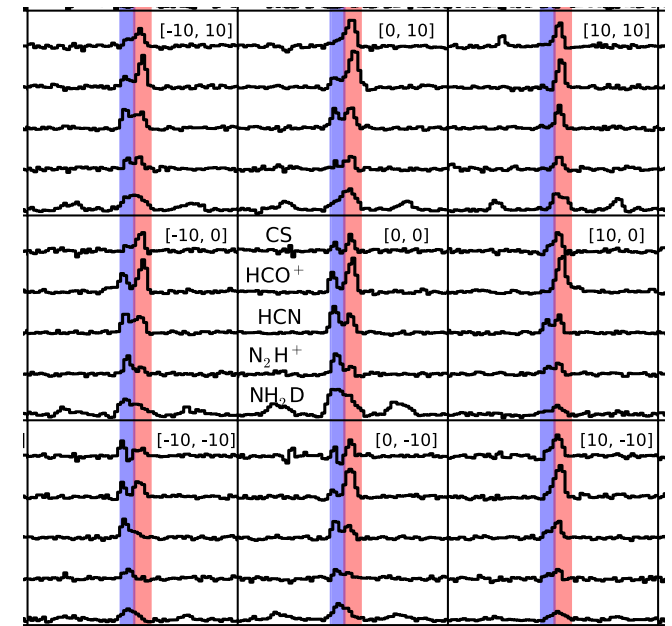


Figure 2. Integrated intensity maps of different species toward Per-bolo 58. The integration velocity range is  $[7, 8.1] \text{ km s}^{-1}$ . This velocity range was chosen to include the main spectral components among the hyperfine line components. Black contours start at  $3\sigma$  and increase in steps of  $3\sigma$  for CS (2-1) and  $7\sigma$  for the rest. White contours show the 3 mm continuum at  $2\sigma$  and  $3\sigma$  (see Table 1). The blue and red arrows show the direction and extent of the blue and red lobe outflow emission in Dunham et al. (2011).

## 1. ラインプロファイル：

2つのピークを持ち、 $0.4\text{-}0.6 \text{ km s}^{-1}$  離れている



### 3. N<sub>2</sub>H<sup>+</sup>の形状・スペクトルをMHDシミュレーションの結果と比較

collapse開始から0.13と0.15 Myr@edge on  
プロファイルは2つの速度成分を持つ

観測結果と一致

2つの速度成分：

非対称ガス分布のエンベロップで生じている

↑この非対称性は乱流起因 in シミュレーション

turbulent&magnetized collapse： コアの観測的特徴の解釈として妥当

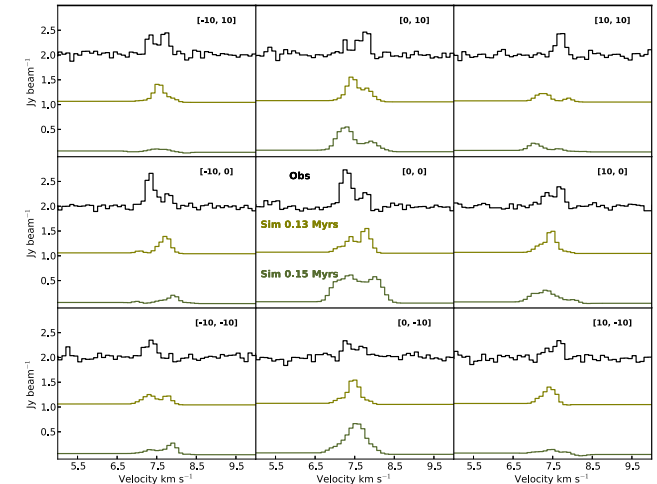
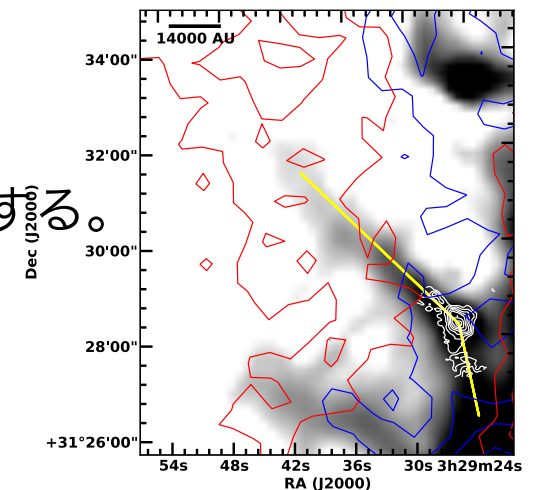


Figure 8. N<sub>2</sub>H<sup>+</sup> (1-0) spectra at different offsets (in arcseconds) from the continuum peak position (Per-bolo 58; black) and center position (simulations; green). The simulated spectra correspond to the edge-on view data cube in Figure 7, where light green and dark green correspond to the time steps 0.13 and 0.15 Myr, respectively.

4. large scale (>0.1 pc) フィラメント降着による、1000auスケールでのガスの非対称性  
についても議論

N<sub>2</sub>H<sup>+</sup>のemission： C<sup>18</sup>Oのフィラメント構造の中にあり、  
コアスケールでの2つの速度成分と一致する。

2つの速度成分はフィラメントスケールからの  
降着の結果の可能性もある



# #40 The Seahorse Nebula: New views of the filamentary infrared dark cloud G304.74+01.32 from SABOCA, *Herschel*, and WISE\*

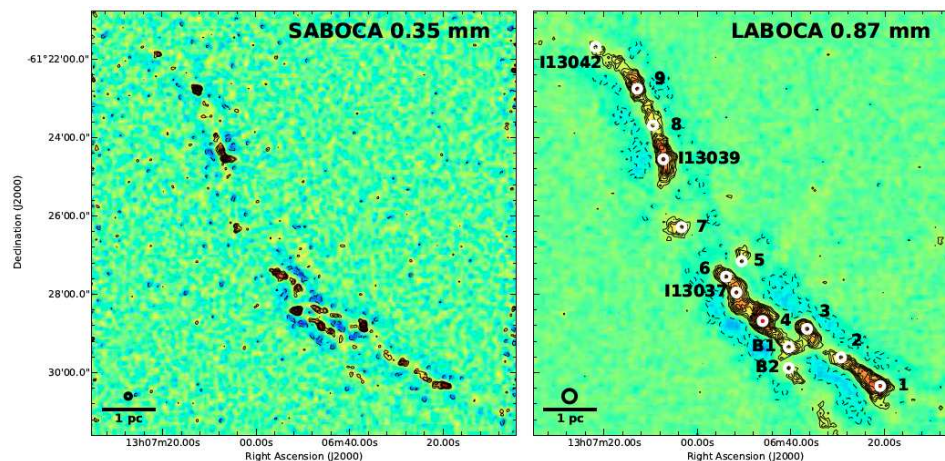
O. Miettinen<sup>1, 2, 3</sup>

Filamentary cloud (例: IRDCs) : 階層的なfragmentationを経て、クランプやコア、星へとなる。

目的:

- ・ IRDC G304.74+01.32のクランプ中での、コアへのfragmentationを見つける
- ・ クランプやコアの物理量も求めたい

観測: SABOCA bolometerを使った $350\mu\text{m}$ のマッピング (分解能 $\sim 9''$ ) + *Herschel* & WISE



LABOCAクランプの36% : SABOCAコアへと分裂

WISEデータから:

SABOCAコアの65%にYSOが付随 (残りはprestellar core候補天体)

**Fig. 1.** SABOCA  $350\mu\text{m}$  (left) and LABOCA  $870\mu\text{m}$  (right) images of G304.74. In both panels, the colour scale is linear. The contours levels start from  $3\sigma$ , and progress in steps of  $1\sigma$ . The dashed contours show the negative features at the  $-3\sigma$  level. The identified clumps are labelled on the LABOCA map, where the numbers refer to the SMM IDs (e.g. 1 means SMM 1), while the sources I13037, I13039, and I13042 are the three *IRAS* sources in the filament. The white circles indicate the LABOCA peak positions of the clumps (see Sect. 3.1). The identified SABOCA sources are not labelled for legibility purposes (see Sect. 3.2), but they are indicated in the zoom-in images in Fig. 4. A scale bar of 1 pc projected length, and the effective beam size ( $9''$  for SABOCA,  $19''.86$  for LABOCA) are shown in the bottom left corner.

SABOCAコア      LABOCAクランプ

|                     |                                      |                                      |
|---------------------|--------------------------------------|--------------------------------------|
| 平均質量                | 29 Msun                              | 55 Msun                              |
| H <sub>2</sub> 柱密度  | $2.9 \times 10^{22} \text{ cm}^{-2}$ | $2.0 \times 10^{22} \text{ cm}^{-2}$ |
| H <sub>2</sub> 個数密度 | $7.9 \times 10^4 \text{ cm}^{-3}$    | $3.1 \times 10^4 \text{ cm}^{-3}$    |

5. Herschel画像： G304.74は伸びたstriationが付随している  
 => 周辺からのmass accretionが続いている  
 => 周辺媒体の圧力がフィラメントの力学的進化に重要な役割を果たしているかも

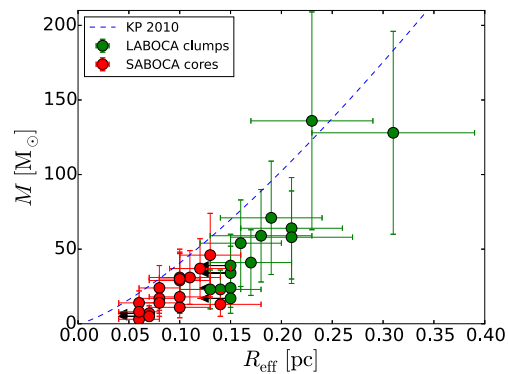


Fig. 5. Masses of the LABOCA clumps and SABOCA cores in G304.74 plotted as a function of their effective radii. The upper size limits are indicated by left pointing arrows. The blue dashed curve represents the mass-radius threshold for high-mass star formation proposed by KP10, that is  $M(R) = 870 M_{\odot} \times (R/\text{pc})^{1.33}$ .

LABOCAクランプの1つだけが  
大質量星形成を示す

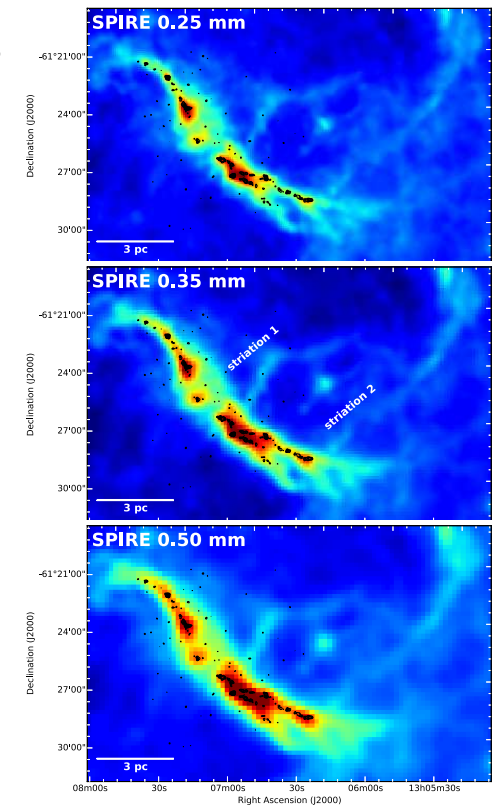


Fig. 2. *Herschel*/SPIRE images of G304.74 and its surroundings. The images are displayed in logarithmic colour-scale to improve the appearance of the low surface brightness features. The overlaid black contours show the SABOCA 350  $\mu\text{m}$  dust continuum emission as in Fig. 1. A scale bar of 3 pc projected length is shown in the bottom left corner of each panel. The two obvious striations are labelled in the middle panel (striation 1 and striation 2).

## #37 The JCMT Transient Survey: Identifying Submillimetre Continuum Variability over Several Year Timescales Using Archival JCMT Gould Belt Survey Observations

Steve Mairs<sup>1,2</sup>, Doug Johnstone<sup>1,2</sup>, Helen Kirk<sup>2</sup>, James Lane<sup>1</sup>, Graham S. Bell<sup>3</sup>, Sarah Graves<sup>3</sup>, Gregory J. Herczeg<sup>4</sup>, Peter Scicluna<sup>5</sup>, Geoffrey C. Bower<sup>6</sup>, Huei-Ru Vivien Chen<sup>7</sup>, Jennifer Hatchell<sup>8</sup>, Yuri Aikawa<sup>9</sup>, Wen-Ping Chen<sup>10</sup>, Miju Kang<sup>11</sup>, Sung-Ju Kang<sup>11</sup>, Jeong-Eun Lee<sup>12</sup>, Oscar Morata<sup>13</sup>, Andy Pon<sup>14</sup>, Aleks Scholz<sup>15</sup>, Satoko Takahashi<sup>16,17</sup> and Hyunju Yoo<sup>12,18</sup>

Investigating variability at the earliest stages of low-mass star formation is fundamental in understanding how a protostar assembles mass. While many simulations of protostellar disks predict non-steady accretion onto protostars, deeper investigation requires robust observational constraints on the frequency and amplitude of variability events characterised across the observable SED. In this study, we develop methods to robustly analyse repeated observations of an area of the sky for submillimetre variability in order to determine constraints on the magnitude and frequency of deeply embedded protostars. We compare 850  $\mu\text{m}$  JCMT Transient Survey data with archival JCMT Gould Belt Survey data to investigate variability over 2-4 year timescales. Out of 175 bright, independent emission sources identified in the overlapping fields, we find 7 variable candidates, 5 of which we classify as *Strong* and the remaining 2 as *Extended* to indicate the latter are associated with larger-scale structure. For the *Strong* variable candidates, we find an average fractional peak brightness change per year of  $|4.0|\% \text{ yr}^{-1}$  with a standard deviation of  $2.7\% \text{ yr}^{-1}$ . In total, 7% of the protostars associated with 850  $\mu\text{m}$  emission in our sample show signs of variability. Four of the five *Strong* sources are associated with a known protostar. The remaining source is a good follow-up target for an object that is anticipated to contain an enshrouded, deeply embedded protostar. In addition, we estimate the 850  $\mu\text{m}$  periodicity of the submillimetre variable source, EC 53, to be  $567 \pm 32$  days based on the archival Gould Belt Survey data.

## #39 Forming spectroscopic massive proto-binaries by disk fragmentation

D.M.-A. Meyer<sup>1</sup>, R. Kuiper<sup>1</sup>, W. Kley<sup>1</sup>, K.G. Johnston<sup>2</sup> and E. Vorobyov<sup>3,4,5</sup>

The surroundings of massive protostars constitute an accretion disc which has numerically been shown to be subject to fragmentation and responsible for luminous accretion-driven outbursts. Moreover, it is suspected to produce close binary companions which will later strongly influence the star's future evolution in the Hertzsprung-Russel diagram. We present three-dimensional gravitation-radiation-hydrodynamic numerical simulations of 100  $M_{\odot}$  pre-stellar cores. We find that accretion discs of young massive stars violently fragment without preventing the (highly variable) accretion of gaseous clumps onto the protostars. While acquiring the characteristics of a nascent low-mass companion, some disc fragments migrate onto the central massive protostar with dynamical properties showing that its final Keplerian orbit is close enough to constitute a close massive proto-binary system, having a young high-mass and a low-mass component. We conclude on the viability of the disc fragmentation channel for the formation of such short-period binaries, and that both processes -close massive binary formation and accretion bursts- may happen at the same time. FU-Orionis-type bursts, such as observed in the young high-mass star S255IR-NIRS3, may not only indicate ongoing disc fragmentation, but also be considered as a tracer for the formation of close massive binaries - progenitors of the subsequent massive spectroscopic binaries - once the high-mass component of the system will enter the main-sequence phase of its evolution. Finally, we investigate the ALMA-observability of the disc fragments.

## #46 Far-infrared to millimeter data of protoplanetary disks: dust growth in the Taurus, Ophiuchus, and Chamaeleon I star-forming regions

Álvaro Ribas<sup>1</sup>, Catherine C. Espaillat<sup>1</sup>, Enrique Macías<sup>1</sup>, Hervé Bouy<sup>2</sup>, Sean Andrews<sup>3</sup>, Nuria Calvet<sup>4</sup>, David A. Naylor<sup>5</sup>, Pablo Riviere-Marichalar<sup>6</sup>, Matthijs H.D. van der Wiel<sup>5,7</sup>, and David Wilner<sup>3</sup>

Far-infrared and (sub)millimeter fluxes can be used to study dust in protoplanetary disks, the building blocks of planets. Here, we combine observations from the Herschel Space Observatory with ancillary data of 284 protoplanetary disks in the Taurus, Chamaeleon I, and Ophiuchus star-forming regions, covering from the optical to mm/cm wavelengths. We analyze their spectral indices as a function of wavelength and determine their (sub)millimeter slopes when possible. Most disks display observational evidence of grain growth, in agreement with previous studies. No correlation is found between other tracers of disk evolution and the millimeter spectral indices. A simple disk model is used to fit these sources, and we derive posterior distributions for the optical depth at 1.3 mm and 10 au, the disk temperature at this same radius, and the dust opacity spectral index. We find the fluxes at 70  $\mu\text{m}$  to correlate strongly with disk temperatures at 10 au, as derived from these simple models. We find tentative evidence for spectral indices in Chamaeleon I being steeper than those of disks in Taurus/Ophiuchus, although more millimeter observations are needed to confirm this trend and identify its possible origin. Additionally, we determine the median spectral energy distribution of each region and find them to be similar across the entire wavelength range studied, possibly due to the large scatter in disk properties and morphologies.

## #47 A Molecular-Line Study of the Interstellar Bullet Engine IRAS05506+2414

Raghvendra Sahai<sup>1</sup>, Chin-Fei Lee<sup>2</sup>, Carmen Sánchez Contreras<sup>3</sup>, Nimesh Patel<sup>4</sup>, Mark Morris<sup>5</sup> and Mark Claussen<sup>6</sup>

We present interferometric and single-dish molecular line observations of the interstellar bullet-outflow source IRAS05506+2414, whose wide-angle bullet spray is similar to the Orion BN/KL explosive outflow and likely arises from an entirely different mechanism than the classical accretion-disk-driven bipolar flows in young stellar objects. The bullet-outflow source is associated with a large pseudo-disk and three molecular outflows – a high-velocity outflow (HVO), a medium-velocity outflow (MVO), and a slow, extended outflow (SEO). The size (mass) of the pseudo-disk is  $10,350 \text{ AU} \times 6,400 \text{ AU}$  ( $0.64\text{--}0.17 M_{\odot}$ ); from a model-fit assuming infall and rotation we derive a central stellar mass of  $8\text{--}19 M_{\odot}$ . The HVO (MVO) has an angular size  $\sim 5180$  ( $\sim 3330$ ) AU, and a projected outflow velocity of  $\sim 140 \text{ km s}^{-1}$  ( $\sim 30 \text{ km s}^{-1}$ ). The SEO size (outflow speed) is  $\sim 0.9 \text{ pc}$  ( $\sim 6 \text{ km s}^{-1}$ ). The HVO's axis is aligned with (orthogonal to) that of the SEO (pseudo-disk). The velocity structure of the MVO is unresolved. The scalar momenta in the HVO and SEO are very similar, suggesting that the SEO has resulted from the HVO interacting with ambient cloud material. The bullet spray shares a common axis with the pseudo-disk, and has an age comparable to that of MVO (few hundred years), suggesting that these three structures are intimately linked together. We discuss several models for the outflows in IRAS 05506+2414 (including dynamical decay of a stellar cluster, chance encounter of a runaway star with a dense cloud, and close passage of two protostars), and conclude that 2nd-epoch imaging to derive proper motions of the bullets and nearby stars can help to discriminate between them.

## #48 Slingshot Mechanism for Clusters: Gas Density Regulates Star Density in the Orion Nebula Cluster (M42)

Amelia M. Stutz<sup>1</sup>

We characterize the stellar and gas volume density, potential, and gravitational field profiles in the central  $\sim 0.5$  pc of the Orion Nebula Cluster (ONC), the nearest embedded star cluster (or rather, proto-cluster) hosting massive star formation available for detailed observational scrutiny. We find that the stellar volume density is well characterized by a Plummer profile  $\rho_{stars}(r) = 5755 M_{\odot} pc^{-3} (1+(r/a)^2)^{-5/2}$ , where  $a = 0.36$  pc. The gas density follows a cylindrical power law  $\rho_{gas}(R) = 25.9 M_{\odot}/pc^3 (R/pc)^{-1.775}$ . The stellar density profile dominates over the gas density profile inside  $r \sim 1$  pc. The gravitational field is gas-dominated at all radii, but the contribution to the total field by the stars is nearly equal to that of the gas at  $r \sim a$ . This fact alone demonstrates that the proto-cluster cannot be considered a gas-free system or a virialized system dominated by its own gravity. The stellar proto-cluster core is dynamically young, with an age of  $\sim 2$ -3 Myr, a 1D velocity dispersion of  $\sigma_{obs} = 2.6$  km s<sup>-1</sup>, and a crossing time of  $\sim 0.55$  Myr. This timescale is almost identical to the gas filament oscillation timescale estimated recently by Stutz & Gould (2016). This provides strong evidence that the proto-cluster structure is regulated by the gas filament. The proto-cluster structure may be set by tidal forces due to the oscillating filamentary gas potential. Such forces could naturally suppress low density stellar structures on scales  $\gtrsim a$ . The analysis presented here leads to a new suggestion that clusters form by an analog of the "slingshot mechanism" previously proposed for stars.

## #49 Monitoring observations of 6.7 GHz methanol masers

M. Szymczak<sup>1</sup>, M. Olech<sup>1</sup>, R. Sarniak<sup>1</sup>, P. Wolak<sup>1</sup> and A. Bartkiewicz<sup>1</sup>

We report results of 6.7 GHz methanol maser monitoring of 139 star-forming sites with the Torun 32 m radio telescope from June 2009 to February 2013. The targets were observed at least once a month, with higher cadences of 2-4 measurements per week for circumpolar objects. Nearly 80 per cent of the sources display variability greater than 10 per cent on a time-scale between a week and a few years but about three quarters of the sample have only 1-3 spectral features which vary significantly. Irregular intensity fluctuation is the dominant type of variability and only nine objects show evidence for cyclic variations with periods of 120 to 416 d. Synchronised and anti-correlated variations of maser features are detected in four sources with a disc-like morphology. Rapid and high amplitude bursts of individual features are seen on 3-5 occasions in five sources. Long (>50 d to 20 months) lasting bursts are observed mostly for individual or groups of features in 19 sources and only one source experienced a remarkable global flare. A few flaring features display a strong anti-correlation between intensity and line-width that is expected for unsaturated amplification. There is a weak anti-correlation between the maser feature luminosity and variability measure, i.e. maser features with low luminosity tend to be more variable than those with high luminosity. The analysis of the spectral energy distribution and continuum radio emission reveals that the variability of the maser features increases when the bolometric luminosity and Lyman flux of the exciting object decreases. Our results support the concept of a major role for infrared pumping photons in triggering outburst activity of maser emission.

## #50 Outflow-Confined HII regions. II. The Early Break-Out Phase

Kei E. I. Tanaka<sup>1</sup>, Jonathan C. Tan<sup>1</sup>, Jan E. Staff<sup>2</sup> and Yichen Zhang<sup>3</sup>

In this series of papers, we model the formation and evolution of the photoionized region and its observational signatures during massive star formation. Here we focus on the early break out of the photoionized region into the outflow cavity. Using results of 3-D magnetohydrodynamic-outflow simulations and protostellar evolution calculations, we perform post-processing radiative-transfer. The photoionized region first appears at a protostellar mass of  $m_* = 10M_\odot$  in our fiducial model, and is confined to within 10–100 AU by the dense inner outflow, similar to some observed very small hyper compact HII regions. Since the ionizing luminosity of the massive protostar increases dramatically as Kelvin-Helmholz (KH) contraction proceeds, the photoionized region breaks out to the entire outflow region in  $\lesssim 10,000$  yr. Accordingly, the radio free-free emission brightens significantly in this stage. In our fiducial model, the radio luminosity at 10 GHz changes from 0.1 mJy kpc<sup>2</sup> at  $m_* = 11M_\odot$  to 100 mJy kpc<sup>2</sup> at  $m_* = 16M_\odot$ , while the infrared luminosity increases by less than a factor of two. The radio spectral index also changes in the break-out phase from the optically thick value of  $\sim 2$  to the partially optically thin value of  $\sim 0.6$ . Additionally, we demonstrate that short-timescale variation in free-free flux would be induced by an accretion burst. The outflow density is enhanced in the accretion burst phase, which leads to a smaller ionized region and weaker free-free emission. The radio luminosity may decrease by one order of magnitude during such bursts, while the infrared luminosity is much less affected, since internal protostellar luminosity dominates over accretion luminosity after KH contraction starts. Such variability may be observable on timescales as short 10–100 yr, if accretion bursts are driven by disk instabilities.